

Large-Scale Fabrication, 3D Tomography, and Lithium-Ion Battery Application of Porous Silicon

Mingyuan Ge,[†] Yunhao Lu,[‡] Peter Ercius,[§] Jiepeng Rong,[†] Xin Fang,[†] Matthew Mecklenburg,^{||} and Chongwu Zhou^{*,†}

[†]Department of Electrical Engineering and Department of Chemical Engineering and Materials Science, University of Southern California, Los Angeles, California 90089, United States

[‡]Department of Materials Science and Engineering, Zhejiang University, Hangzhou, Zhejiang 310027, P. R. China

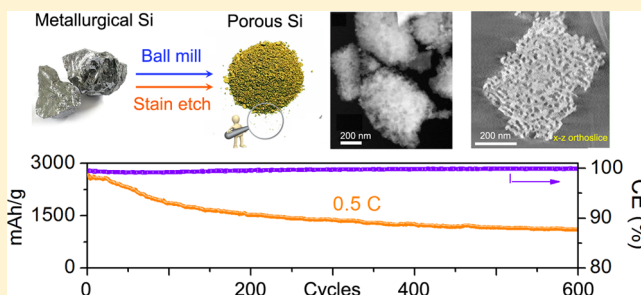
[§]National Center for Electron Microscopy, Lawrence Berkeley National Laboratory, Berkeley, California 94720, United States

^{||}Center for Electron Microscopy and Microanalysis, University of Southern California, Los Angeles, California 90089, United States

S Supporting Information

ABSTRACT: Recently, silicon-based lithium-ion battery anodes have shown encouraging results, as they can offer high capacities and long cyclic lifetimes. The applications of this technology are largely impeded by the complicated and expensive approaches in producing Si with desired nanostructures. We report a cost-efficient method to produce nanoporous Si particles from metallurgical Si through ball-milling and inexpensive stain-etching. The porosity of porous Si is derived from particle's three-dimensional reconstructions by scanning transmission electron microscopy (STEM) tomography, which shows the particles' highly porous structure when etched under proper conditions. Nanoporous Si anodes with a reversible capacity of 2900 mAh/g was attained at a charging rate of 400 mA/g, and a stable capacity above 1100 mAh/g was retained for extended 600 cycles tested at 2000 mA/g. The synthetic route is low-cost and scalable for mass production, promising Si as a potential anode material for the next-generation lithium-ion batteries with enhanced capacity and energy density.

KEYWORDS: Cost-efficient, porous silicon, lithium-ion battery, 3D tomography



The development of lithium-ion batteries with lightweight and high-energy density has been a topic of intense research. Recently, driven by the demands of electric vehicles (EV) and hybrid electric vehicles (HEV), academia and industry seek to advance the capacity and cyclic life of electrode materials for the next-generation lithium-ion batteries.^{1–3} In contrast to traditional graphite anodes where six carbon atoms bond to only one lithium atom, Si is advantageous because each Si atom can bond up to 3.75 lithium atoms, making Si a promising anode replacement to graphite. The stoichiometry of Li–Si alloy allows a theoretical capacity of 3600 mAh/g for Si, which is almost 10 times larger than the capacity of graphite.⁴ However, a large volume change (~300%) of Si upon insertion and extraction of lithium ions leads to severe electrode pulverization and capacity degradation, bringing important concerns regarding the long-time stability and lifetime of Si anodes. Recently, pioneering work by Cui et al.⁵ and others^{6–21} have shown that engineering Si into nanostructures promises an effective strategy to alleviate the pulverization problem by accommodating the volume expansion and reducing the stress to prevent material rupture. Encouraging results have been reported on a variety of nanostructured Si such as Si nanoparticles,^{6,7} nanowires,^{5,8}

nanotubes,^{9–12} and nanoporous Si.^{13–22} While significant progress on Si anodes has been made to achieve high performance, the production of nanostructured Si that involves high-temperature pyrolysis of toxic and expensive silane precursor (~\$50 000/ton) limits the practical applications of Si anodes.^{5,17,23–28} It is highly desirable to develop strategies producing Si nanostructures with a production cost similar to graphite to generate real impact to the adoption of Si as lithium battery anodes.

Metallurgical Si is an attractive material choice because of its abundance and cheap price (~\$1000/ton). It has prevalence in the electronics and PV industries; however, few reports have described for energy storage applications. Here we report on converting metallurgical Si into porous Si particles with a high specific area and high porosity through a ball-milling and stain etching process for use as lithium-ion battery anodes. The internal structure of the porous Si particles was extensively characterized by scanning transmission electron microscopy (STEM) tomography—an imaging method allowing a three-

Received: October 20, 2013

Revised: November 21, 2013

dimensional reconstruction of objects—to disclose the highly porous features of the particles. STEM tomography provides a direct measurement of the porous structure for different synthesis conditions, which is then compared to their performance as a battery anode. Electrochemical tests have demonstrated that lithium-ion battery anodes constructed of nanoporous Si particles obtained under proper reaction conditions can deliver a stable capacity of 2900 mAh/g at a charging rate of 400 mA/g (0.1 C) with 10 cycles measured and a capacity above 1100 mAh/g at 2000 mA/g (0.5 C) with extended 600 cycles measured.

Material Preparation and Structure Characterization.

A schematic diagram of synthesizing porous Si from bulk metallurgical Si is presented in Figure 1A. In a typical

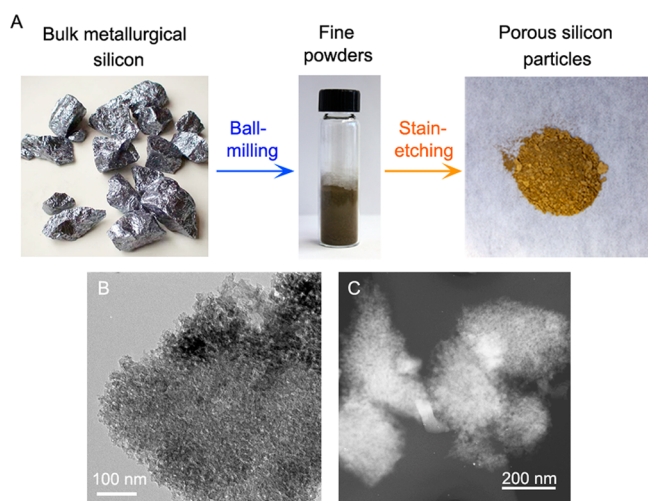


Figure 1. Schematic diagram of the synthesis and morphology of porous silicon particles. (A) Synthetic route of porous silicon from metallurgical silicon through ball-milling and stain-etching. (B) A TEM image of porous Si particles. (C) A STEM image of porous Si particles.

experiment, metallurgical-grade Si (Elkem Inc.) was used as received. The purity of the Si is approximately 99.2%, where iron and aluminum are the two major impurities as indicated by the supplier. The large metallurgical Si particles were first ground to obtain a fine powder using a ball-mill (MTI Inc., 300 W) operated at a grinding speed of 1200 rpm for 5 h, in which the ball milling is a mature and energy-efficient technology in producing micrometer- or submicrometer-particles. The ground powder has a dark-brown color with feature sizes of $\sim 1\ \mu\text{m}$ measured using scanning electron microscopy (SEM) (Supplementary Figure S1). After ball milling, impurity concentrations of Fe and Al were measured using an inductively coupled plasma atomic emission spectrometer (ICP-AES), showing the concentrations of Fe and Al being 1.9% and 0.47%, respectively. The Si powder was then soaked in ferric etchant (named stain etching) containing 30 mM $\text{Fe}(\text{NO}_3)_3$ and 5 M HF with an additional small amount of ethanol under continuous stirring to suppress the forming of a floated foam due to the hydrophobic nature of hydrogen-terminated Si. After 2 h of reaction, precipitates containing porous Si particles were collected and washed for further characterization (samples from this etching condition are denoted as porous Si(1)). The yield of porous silicon in this production process is around 30%. It was found that the overall porous silicon particles have a

Brunauer–Emmett–Teller (BET) surface area of $70\ \text{m}^2/\text{g}$ with pore diameter distribution peaked around 3 nm analyzed by Barrett–Joyner–Halenda (BJH) measurements (Supplementary Figure S2). Figure S3 in the Supporting Information shows the X-ray diffraction (XRD) pattern of porous Si(1); the domain size can be calculated using the Scherrer formula, which gives an average domain size of 19 nm.

The TEM image (as in Figure 1B) was initially used to characterize the porosity of the particles, but such projection images are difficult to interpret due to overlapping internal features. Electron tomography is a microscopy technique that recovers the three-dimensional structure of an object from a series of projection images at different viewing angles. Here, high-angle annular dark field (HAADF) STEM (Figure 1C), which provides projection images with intensity proportional to the projected thickness of the Si particles, was used to quantitatively characterize the porous structure of Si in three dimensions in the following study. The measured porosity throughout the particle agrees well with the high surface area ($70\ \text{m}^2/\text{g}$) analyzed by BET.

We attribute the success of making porous Si particles through a simple etching method to the unique properties of metallurgical Si in terms of unintentional high impurity densities, as well as the selection of etchant components. A mechanistic study of the porous Si formation is interesting and will be beneficial to optimizing the porous structure for various applications.

As confirmed by ICP-AES measurements, Fe and Al are the two major impurities in the metallurgical Si used in these experiments. From first principle calculations, the projected density of states (PDOS) of Fe, Al, and Si were calculated based on the anatomic model of Fe- and Al-doped Si (part of the atomic model is shown in Figure 2A).²⁹ It was found that the electrons from both Fe and Al atoms form a continuous defect band around the Fermi level of pure Si, while Fe contributes more states than Al does in the middle of the band gap (Figure 2B). When the particles are immersed in the stain etchant, the etchant solution acts as hole reservoir, wherein both Fe^{3+} and NO_3^- oxidize Si by donating holes to the defect bands, as illustrated in the schematic diagram in Figure 2C. Our calculations indicate that the electrons corresponding to the defect bands are highly localized: electrons possessing energy within $\pm 0.5\ \text{eV}$ around the Fermi level are spatially localized around the Fe atoms (yellow part in Figure 2D), and therefore etchant species like Fe^{3+} and NO_3^- are energetically favorable to inject holes to the defect sites (e.g., Fe doping sites) to induce etching and leave void space on Si. After etching, the concentration of Fe impurity in silicon is reduced to a negligible level (less than 0.1%) as determined by ICP-AES measurements.

During the etching process, several reactions occur simultaneously. Oxidation of Si with Fe^{3+} is straightforward; however, NO_3^- has a complex behavior in the presence of H^+ (see the Supporting Information). To isolate the roles that Fe^{3+} and NO_3^- played during the etching process, control experiments were carried out to substitute $\text{Fe}(\text{NO}_3)_3$ with FeCl_3 in the etchant (samples from this etch condition are denoted as Si(2)). Figure 3 compares the morphologies of the porous Si (Si(1) and Si(2)) obtained from the two different etching conditions. HAADF-STEM projection images of Si(1) (Figure 3A) and Si(2) (Figure 3F) show that both materials are porous. BET measurements of Si(1) and Si(2) determined that the exposed (external and internal) surface areas of the

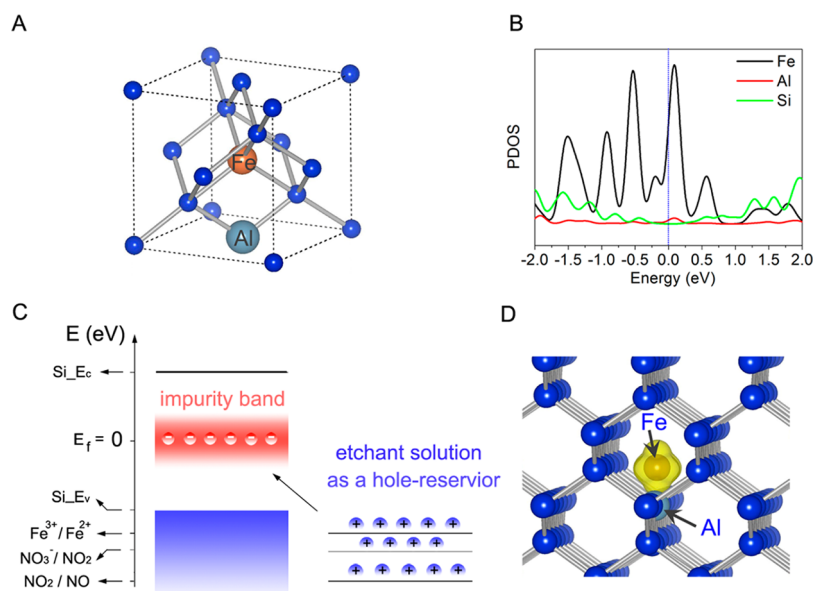


Figure 2. Mechanism of stain-etching to prepare porous silicon. (A) Part of the atomic model containing Fe–Al dopants in silicon used in first-principle calculations. The whole atomic model is a $3 \times 3 \times 3$ supercell of silicon conventional cell. (B) First-principle calculations of projected density of states of Fe, Al, and Si atoms. (C) Schematic diagram of band alignment of silicon and different redox pairs. The etchant solution functions as a hole reservoir and can inject holes into the impurity band of silicon. (D) Calculated spatial distribution of electrons with energy within ± 0.5 eV of Fermi energy. The yellow part indicates that the electron within this energy is mostly localized around the Fe atom.

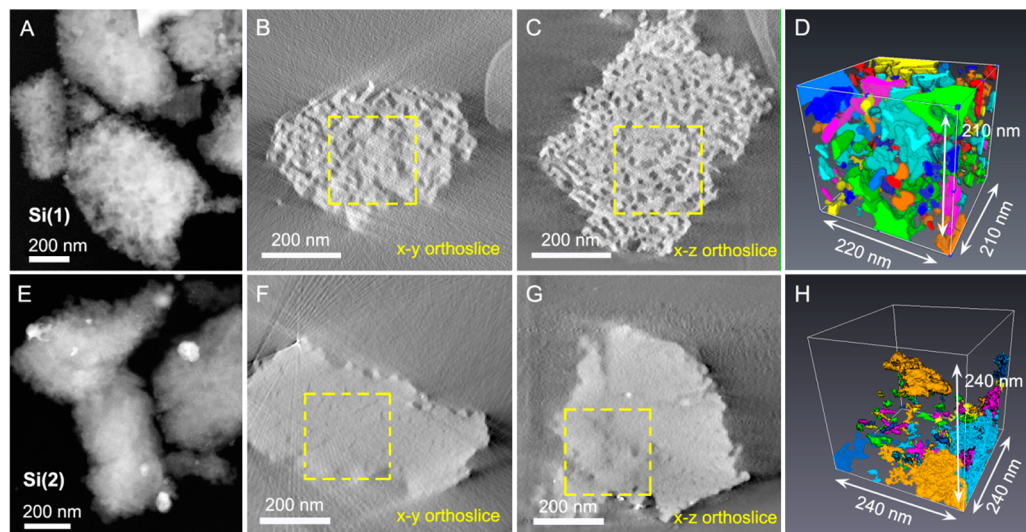


Figure 3. Structure characterization of Si(1) and Si(2). HAADF-STEM images of Si(1) and Si(2) are shown in A and E. Si(1) and Si(2) are reconstructed from HAADF-STEM tomography shown in B–D and F–H, respectively. Orthogonal central slice views of Si(1) corresponding are shown in B–C (for Si(1)) and F–G (for Si(2)). 3D pore connections corresponding to the square region in B–C and F–G are reconstructed and shown in D and H for Si(1) and Si(2), respectively; labeled colors indicate the separated pore connections.

materials are $70 \text{ m}^2/\text{g}$ and $19 \text{ m}^2/\text{g}$, and the pore volumes are $0.133 \text{ cm}^3/\text{g}$ and $0.036 \text{ cm}^3/\text{g}$, respectively, suggesting a much lower porosity of Si(2). STEM tomography was applied to reconstruct the 3D porous structure of Si(1) and Si(2) to reveal their structure difference. Orthogonal central slices of the 3D particle reconstructions shown in Figure 3B–C for Si(1) and Figure 3F–G for Si(2) clearly reveal the difference between the two porous networks: Si(1) is porous throughout the whole particle; Si(2) has a porous surface and a more solid core. The porosity of Si(1) and Si(2) was derived from the reconstructed structures by separating pores from their surrounding solid structures based on the contrast difference in each sliced view of 3D reconstructions derived from

HAADF-STEM images. The reconstructed pore connections are shown in Figure 3D and H for Si(1) and Si(2), respectively. The uniformly distributed pores in Si(1) are in sharp contrast to the partially dispersed pores in Si(2). The pore volumes were calculated, and porosities for Si(1) and Si(2) were derived to be $22 \pm 3\%$ and $4 \pm 2\%$, respectively; the specific surfaces were also calculated to be $150 \pm 30 \text{ m}^2/\text{g}$ and $40 \pm 20 \text{ m}^2/\text{g}$ correspondingly, which agrees well with the measured value ($70 \text{ m}^2/\text{g}$ for Si(1) and $19 \text{ m}^2/\text{g}$ for Si(2)).

Comparison of porous structures of Si(1) and Si(2) suggest that NO_3^- has an increased effect to the formation of a connected porous structure. In the presence of HF, weakly dissociated H^+ can increase the redox potential of NO_3^- to

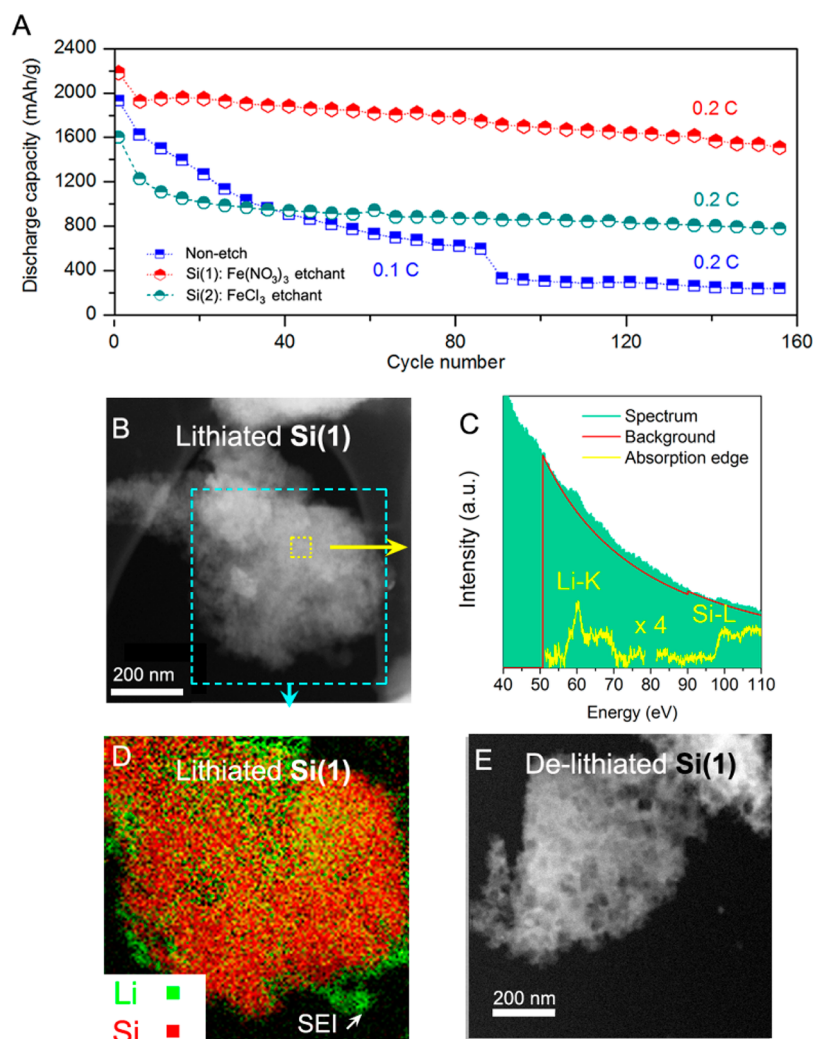


Figure 4. Electrochemical measurements and structure characterization of porous silicon nanoparticles. (A) Cyclic performance of porous silicon of unetched silicon, Si(1), and Si(2) at a current rate of 0.2 C. (B) An ex situ STEM image showing the morphology of Si(1) after the first lithiation. The porous feature of the lithiated particle demonstrates the capability of porous structure to accommodate volume expansion during the lithiation process. (C) EELS spectrum showing the formation of Li_xSi . (D) Li and Si mapping derived from EELS spectra in the blue square region of B. (E) An ex situ STEM image shows the morphology of Si(1) after 10 cycles and being charged to 2 V (delithiated state). The particle maintains its integrity without cracking.

assist the oxidation of Si at the defect sites. Further increasing H^+ concentration by adding additional HNO_3 to the etchant, however, does not significantly affect the particle morphology (Supplementary Figure S4e–h); however the yield of particles decreases. This might be attributed to the strong oxidation ability of NO_3^- at a high H^+ concentration, which leads etching of the Si at and also away from the defect sites. To further check the effect of impurities to the formation of porous structure, undoped silicon nanoparticles (purchased from Alfa) were etched under the same etching condition. Results show that these particles remained solid (Supplementary Figure S5), clearly revealing the critical role that impurities (e.g., the Fe in metallurgical Si) played in the formation of porous silicon.

Electrochemical Performance. The electrochemical performances of porous Si as lithium-ion battery anodes were examined using a half-cell configuration. All samples were coated with carbon and then coated with graphene oxide (GO) to increase the electrical conductivity of electrodes (denoted as Si@GO, Si accounts for 95 wt %). The average mass loading of is 1.2 mg/cm², wherein the mass ratio of Si@GO–carbon

black–binder = 7:2:1. Here, carbon black is still used, because the small conductive carbon black particles would fill into the void space between the relative large silicon particles to increase conductive paths. The calculated tap density of electrodes is around 0.54 g/cm³ based on the weight of Si (Supporting Information), and cell capacities are calculated based on the total weight of Si with carbon and GO coating. Figure 4A compares the cyclic performance of Si(1), Si(2), and unetched Si powders. There was severe capacity degradation for the unetched Si when the battery was tested at a current rate of 0.1 C (1 C = 4000 mAh/g). Furthermore, the capacity of unetched Si quickly dropped to 200 mAh/g when the current rate was increased to 0.2 C. Porous Si (e.g., Si(2), etched using FeCl_3/HF) showed much improved cyclic performance, as it could deliver stable capacity >800 mAh/g after 160 cycles at a 0.2 C rate.

Si(1) showed even better performance than Si(2). The capacity of Si(1) retained >1400 mAh/g at a current rate of 0.2 C for 160 cycles. It is not surprise that Si with a higher porosity has better performance. On one hand, a particle with high

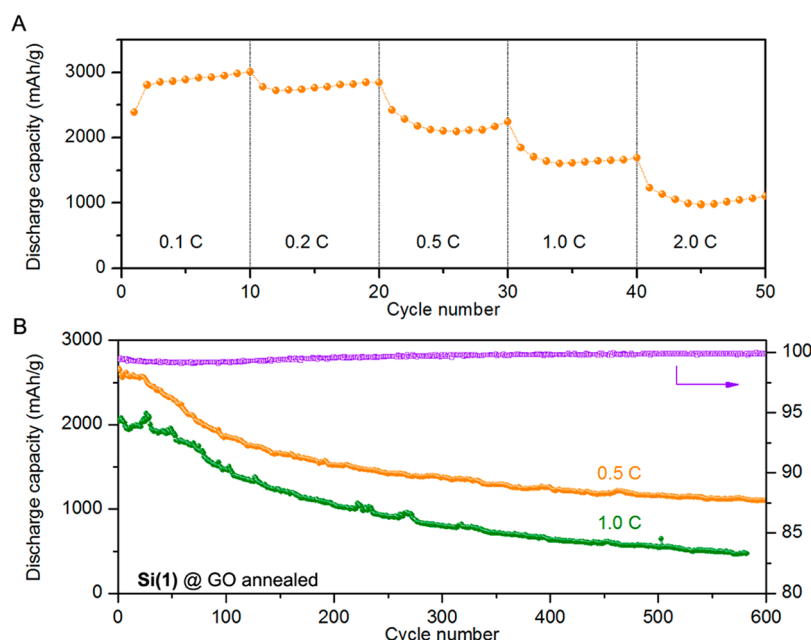


Figure 5. Electrochemical measurements of porous silicon **Si(1)** (coated with carbon and graphene oxide) after annealing in Ar at 700 °C. (A) Discharge capacity of the samples at different current rates. (B) Cyclic performance of the samples at current rates of 0.5 and 1.0 C (note: samples are precharged/discharged at 0.1 C for 10 cycles). The Coulombic efficiency stabilizes above 99% for all cycles (the Coulombic efficiency curve is for a sample cycled at 0.5 C).

porosity can provide large void space allowing for volume expansion during the lithiation process. On the other hand, porous Si is more “flexible” to withstand structure deformation than solid Si under external or internal stress to maintain its structure integrity. One indicative evidence comes from nanoindentation experiment, which indicates a rather low Young’s modulus 2.4 ± 0.3 GPa of **Si(1)** compared to bulk Si (see the Supporting Information). The small Young’s modulus arises from the plastic-like deformation of the porous structure³⁰ (Supplementary Figure S7), which will help to keep electrode integrity without losing electric contact. Another merit of porous structure lies on the large surface area and therefore a larger particle–electrolyte interface to facilitate fast intercalation of Li^+ ions into Si to improve the rate performance at high current density. For example, the apparent Li^+ ion diffusion rates are 3.4×10^{-13} m²/s for **Si(1)** and 6.8×10^{-14} m²/s for **Si(2)** using a potentiostatic intermittent titration technique.³¹ The diffusion rate difference reflects the particle geometry effect, as particles with higher surface area allow more Li^+ ions diffusing into the body at a given time interval.

To better understand the electrode stability under cyclic charge–discharge test, ex situ TEM studies of porous Si particles **Si(1)** were carried out to characterize the morphology evolution in lithiated and delithiated states. STEM image in Figure 4B clearly shows the porous feature of particle remained at the lithiated state without initiating any cracks. The formation of Li_xSi is also characterized by electron energy loss spectra (EELS). Figure 4C shows the typical EELS spectrum summed over the square region in Figure 4B in the 40–120 eV range. A total of 64×64 EELS spectra were acquired with a bandwidth suited to detecting the Li and Si core-loss edge. Energy loss windows of 57–70 eV for Li and 99–110 eV for Si were used to calculate the integral core-loss signals after appropriate background subtraction. The coexistence of Si and Li in Figure 4D implies the formation of Li_xSi . A Li-rich region detected at the particle’s periphery indicates

the formation of solid–electrolyte interface (SEI). This well-formed SEI layer can protect the electrode material from further degradation under cyclic measurement, which is crucial to maintaining electrode capacity at extended cycles. A close examination of EELS spectra at different positions can be found in Figure S4 in the Supporting Information. For the delithiated state, Figure 4e shows that the particle turns back into the highly porous structure without breaking into pieces. The structural integrity retained in both the lithiated and the delithiated states demonstrates the capability of a porous Si structure to accommodate a large volume expansion and a stable solid–electrolyte interface, thus promoting the battery performance at long cyclic life.

The performance of Si@GO (Si from **Si(1)**) can be further improved by annealing the samples before assembling into a battery, as the conductivity of GO can be dramatically increased when annealed at high temperatures compared with using chemical reduction methods.³¹ As shown in Figure 5A, the samples annealed at 700 °C show excellent performance: the capacity stabilized at different current rates from 2900 mAh/g at 0.1 C to 1000 mAh/g at 2 C. The volumetric capacity (product of gravimetric capacity and tap density) is calculated to be 1500 mAh/cm³ at 0.1 C and 540 mAh/cm³ at 2 C, which is comparable to a recently reported silicon anode work.³² Figure 5B shows the discharge capacity of the same sample at extended cycles. The capacity remained above 1100 mAh/g and 550 mAh/g at rates of 0.5 and 1.0 C over 600 cycles, respectively. The Coulombic efficiency was 83% for the first cycle and 98% for the second cycle, then gradually increased to over 99% after five cycles (Supplementary Figure S10A), and remained stable for the rest of cyclic tests. The relatively low Coulombic efficiency for the first several cycles might arise from the SEI formation and the use of graphene oxide. The voltage profile for selected cycles can be found in Supplementary Figure S10B.

Table 1. Comparisons of the Properties and Performance of Porous Si(1) and Si(2)

	porosity (calculated)	surface area (m ² /g)		Li ⁺ diffusion rate (m ² /s)	Young's modulus (GPa)	capacity (mAh/g)
		BET	calculated			
Si(1)	22 ± 3%	70	150 ± 30	3.4×10^{-13}	2.4 ± 0.3	1400
Si(2)	4 ± 2%	19	40 ± 20	6.8×10^{-14}	similar to bulk Si	800

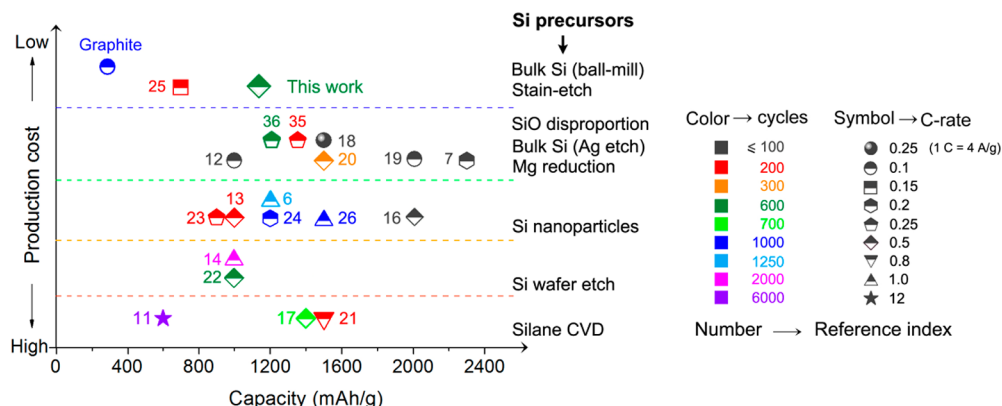


Figure 6. Evaluation of silicon anodes in terms of capacity, cycle number, current rate, and production cost. The color scheme represents the cycle number; the symbol represents the current rate; the numbers next to each symbol refer to the reference index.

Discussion. The battery performance of Si is known to be highly correlated with its structure. Table 1 summarizes some key features of the porous Si studied in this work. The high porosity, large surface area, fast lithium-ion diffusion rate, and the ability of a certain amount of plastic deformation contribute to the overall stable performance of Si anode. One may notice that the large surface area of porous silicon may contribute to a large amount of SEI formation, which would lead to a low Coulombic efficiency of the first several cycles. In this work, we find that carbon coating on silicon surface mitigates the problem to a certain degree. The porous silicon with carbon coating even has a higher first cycle Coulombic efficiency (83%) than nonporous silicon anodes without carbon coating previously reported.³³

For traditional graphite–LiFePO₄ systems, Fe is known to have an adverse effect on the graphite anode,³⁴ as metal Fe particles may be formed from the dissolution of the Fe from LiFePO₄ cathode and then deposit on the graphite surface. These Fe particles would catalyze a formation of interfacial film on the surface of graphite, leading to an increase of electrode impedance and degradation of electrode performance. In the porous silicon anode we studied here, the low concentrations of Fe impurities are well-distributed in the silicon, which is different from Fe particles formed on graphite surface. We therefore expect minimal side effects from the Fe impurities on the operation of porous silicon electrode. A further study will be carried out to fully understand this issue.

We believe the improved battery performance combined with the simplicity of the synthetic method using inexpensive metallurgical Si and inexpensive etchants will advance the potential of Si anodes for real battery applications. Compared with other reported work on Si anodes, the proposed porous Si offers many advantages over other structures in battery research and other fields: (i) Metallurgical Si is the cheapest Si material available with a price (~\$1000/ton) comparable to battery-grade graphite, and the abundance of metallurgical Si fulfills the prerequisite for scalable production. (ii) The ball-milling technology employed is a mature technology, simple, eco-

friendly, and energy efficient. (iii) Ferric nitrate/hydrofluoric acid (Fe(NO₃)₃/HF) etchant has a similar oxidant potential as Ag⁺ (from AgNO₃, commonly used in metal assisted electroless etching) but is less expensive. In addition, the approach used in this study stands as a generic method to prepare porous Si (or germanium) particles from different starting materials. For example, Si nanoparticles have been successfully converted into porous nanoparticles, as shown in Supplementary Figure S11, which may find broad applications in multiple disciplines, such as catalysis, biosensing, and drug delivery. (iv) STEM tomography is demonstrated as a powerful tool to visualize the internal structure of nanoscale materials to make direct, quantitative measurements of similar structures to compare against different materials properties. Particularly in this work, STEM tomography helps to determine the connection between etching conditions, material structure, and battery performance.

Figure 6 compares the Si anode performance from this work and some recent progress.^{6,11–14,17,18,20,21,23–27,35,36} The approach in this study compares more favorable than many other approaches in the production cost. For example, while the reported capacity of porous Si prepared through a disproportionation reaction of SiO is comparable to our results, SiO is of higher price than the metallurgical Si studied in this work, and the disproportionation of SiO at high temperature requires a large thermal budget.^{35,36}

We believe further optimization of porous structures will lead to an even higher capacity and longer cyclic life. The study of the compatibility of Si anode with cathode materials such as LiMn₂O₄, LiFePO₄, and sulfur also deserves further endeavors to harvest the full potential of the porous Si anodes.

In conclusion, we have developed a low-cost and scalable approach to prepare porous Si particles from bulk metallurgical Si. The impurities inside the Si have a profound effect on the formation of porous structure when using Fe(NO₃)₃/HF as an etchant. An extensive study on the STEM tomography reconstruction reveals the highly porous feature of Si particles under proper etching conditions. Electrodes making use of porous Si particles have shown encouraging battery perform-

ance, as they can achieve stable capacity of 2900 mAh/g at a charging rate of 0.1 C with 10 cycles measured and capacity above 1100 mAh/g at 0.5 C with extended 600 cycles measured. The overall performance is superior to the materials prepared by many other synthetic approaches, especially in terms of the production cost. We anticipate that this method will boost the development of Si anode toward real applications.

Methods. 3D Tomography and Structure Characterization. For 3D tomography, HAADF-STEM images were taken at TECNAI F20 in the National Center for Electron Microscopy at the Lawrence Berkeley Laboratory. HAADF-STEM images were recorded at single rotation from -75° to 75° at 1° interval. A total of 151 images were aligned using ETOMO to reconstruct the 3D structure of particles. Other STEM and TEM images were recorded at JEOL 2100F at Center for Electron Microscopy and Microanalysis at the University of Southern California.

Electrode Fabrication. Porous Si particles (Si(1), Si(2)) were first coated with carbon using C_2H_4 as a gas source and Ar as carrier gas under $860^\circ C$ for 10 min. Graphene oxide (GO) was then mixed with particles in water solution, followed by reduction using hydrazine at $90^\circ C$ for 20 min. Thermal annealed samples were made by annealing the samples at $700^\circ C$ using H_2 (5% diluted in Ar) as carrier gas for 20 min. The porous Si electrodes were fabricated by pasting the slurry (Si-carbon-black-alginate acid sodium salt = 7:2:1 by weight) on a copper foil and then dried at $90^\circ C$ for 6 h. Later, coin cells were assembled using a lithium foil as the counter/reference electrode; 1 M LiPF₆ in dimethyl carbonate/fluoroethylene carbonate (1:1 by volume) was used as the electrolyte.

■ ASSOCIATED CONTENT

● Supporting Information

Fe, Al concentration calibration, pore size distribution of porous Si, XRD pattern of porous Si, first-principle calculation, control experiment on nondoped silicon nanoparticles, and nanoindentation on porous Si. This material is available free of charge via the Internet at <http://pubs.acs.org>.

■ AUTHOR INFORMATION

Notes

The authors declare no competing financial interest.

■ ACKNOWLEDGMENTS

We acknowledge the funding support from the University of Southern California. A portion of the images and data used in this article were acquired at The Center for Electron Microscopy and Microanalysis, University of Southern California. We acknowledge support from the National Center for Electron Microscopy, Lawrence Berkeley Laboratory, which is supported by the U.S. Department of Energy under Contract DE-AC02-05CH11231. Y.L. thanks the funding support from National Natural Science Foundation of China (11004171).

■ REFERENCES

- (1) Tarascon, J. M.; Armand, M. Issues and challenges facing rechargeable lithium batteries. *Nature* **2001**, *414*, 359–367.
- (2) Goodenough, J. B.; Kim, Y. Challenges for Rechargeable Li Batteries. *Chem. Mater.* **2010**, *22*, 587–603.
- (3) Etacheri, V.; Marom, R.; Elazari, R.; Salitra, G.; Aurbach, D. Challenges in the development of advanced Li-ion batteries: a review. *Energy Environ. Sci.* **2011**, *4*, 3243–3262.
- (4) Obrovac, M. N.; Christensen, L. Structural changes in silicon anodes during lithium insertion/extraction. *Electrochem. Solid-State Lett.* **2004**, *7*, A93–A96.
- (5) Chan, C. K.; Peng, H. L.; Liu, G.; McIlwrath, K.; Zhang, X. F.; Huggins, R. A.; Cui, Y. High-performance lithium battery anodes using silicon nanowires. *Nat. Nanotechnol.* **2008**, *3*, 31–35.
- (6) Kovalenko, I.; Zdyrko, B.; Magasinski, A.; Hertzberg, B.; Milicev, Z.; Burtovyy, R.; Luzinov, I.; Yushin, G. A Major Constituent of Brown Algae for Use in High-Capacity Li-Ion Batteries. *Science* **2011**, *334*, 75–79.
- (7) Bang, B. M.; Kim, H.; Song, H. K.; Cho, J.; Park, S. Scalable approach to multi-dimensional bulk Si anodes via metal-assisted chemical etching. *Energy Environ. Sci.* **2011**, *4*, 5013–5019.
- (8) Chan, C. K.; Patel, R. N.; O'Connell, M. J.; Korgel, B. A.; Cui, Y. Solution-Grown Silicon Nanowires for Lithium-Ion Battery Anodes. *ACS Nano* **2010**, *4*, 1443–1450.
- (9) Park, M. H.; Kim, M. G.; Joo, J.; Kim, K.; Kim, J.; Ahn, S.; Cui, Y.; Cho, J. Silicon Nanotube Battery Anodes. *Nano Lett.* **2009**, *9*, 3844–3847.
- (10) Song, T.; Xia, J. L.; Lee, J. H.; Lee, D. H.; Kwon, M. S.; Choi, J. M.; Wu, J.; Doo, S. K.; Chang, H.; Il Park, W.; Zang, D. S.; Kim, H.; Huang, Y. G.; Hwang, K. C.; Rogers, J. A.; Paik, U. Arrays of Sealed Silicon Nanotubes As Anodes for Lithium Ion Batteries. *Nano Lett.* **2010**, *10*, 1710–1716.
- (11) Wu, H.; Chan, G.; Choi, J. W.; Ryu, I.; Yao, Y.; McDowell, M. T.; Lee, S. W.; Jackson, A.; Yang, Y.; Hu, L. B.; Cui, Y. Stable cycling of double-walled silicon nanotube battery anodes through solid-electrolyte interphase control. *Nat. Nanotechnol.* **2012**, *7*, 309–314.
- (12) Yoo, J. K.; Kim, J.; Jung, Y. S.; Kang, K. Scalable Fabrication of Silicon Nanotubes and their Application to Energy Storage. *Adv. Mater.* **2012**, *24*, 5452–5456.
- (13) Ge, M.; Rong, J.; Fang, X.; Zhang, A.; Lu, Y.; Zhou, C. Scalable production of porous silicon nanoparticles and their application in lithium-ion battery anode. *Nano Res.* **2012**, *6*, 174–181.
- (14) Ge, M. Y.; Rong, J. P.; Fang, X.; Zhou, C. W. Porous Doped Silicon Nanowires for Lithium Ion Battery Anode with Long Cycle Life. *Nano Lett.* **2012**, *12*, 2318–2323.
- (15) Qu, Y. Q.; Liao, L.; Li, Y. J.; Zhang, H.; Huang, Y.; Duan, X. F. Electrically Conductive and Optically Active Porous Silicon Nanowires. *Nano Lett.* **2009**, *9*, 4539–4543.
- (16) Kim, H.; Han, B.; Choo, J.; Cho, J. Three-Dimensional Porous Silicon Particles for Use in High-Performance Lithium Secondary Batteries. *Angew Chem., Int. Ed.* **2008**, *47*, 10151–10154.
- (17) Yao, Y.; McDowell, M. T.; Ryu, I.; Wu, H.; Liu, N. A.; Hu, L. B.; Nix, W. D.; Cui, Y. Interconnected Silicon Hollow Nanospheres for Lithium-Ion Battery Anodes with Long Cycle Life. *Nano Lett.* **2011**, *11*, 2949–2954.
- (18) Zhao, Y.; Liu, X. Z.; Li, H. Q.; Zhai, T. Y.; Zhou, H. S. Hierarchical micro/nano porous silicon Li-ion battery anodes. *Chem. Commun.* **2012**, *48*, 5079–5081.
- (19) Bang, B. M.; Lee, J. I.; Kim, H.; Cho, J.; Park, S. High-Performance Macroporous Bulk Silicon Anodes Synthesized by Template-Free Chemical Etching. *Adv. Energy Mater.* **2012**, *2*, 878–883.
- (20) Liu, N.; Huo, K. F.; McDowell, M. T.; Zhao, J.; Cui, Y. Rice husks as a sustainable source of nanostructured silicon for high performance Li-ion battery anodes. *Sci. Rep.-U.K.* **2013**, *3*, 7.
- (21) Gowda, S. R.; Pushparaj, V.; Herle, S.; Girishkumar, G.; Gordon, J. G.; Gullapalli, H.; Zhan, X. B.; Ajayan, P. M.; Reddy, A. L. M. Three-Dimensionally Engineered Porous Silicon Electrodes for Li Ion Batteries. *Nano Lett.* **2012**, *12*, 6060–6065.
- (22) Thakur, M.; Sinsabaugh, S. L.; Isaacson, M. J.; Wong, M. S.; Biswal, S. L. Inexpensive method for producing macroporous silicon particulates (MPSPs) with pyrolyzed polyacrylonitrile for lithium ion batteries. *Sci. Rep.-U.K.* **2012**, *2*, 795.
- (23) Wu, H.; Zheng, G. Y.; Liu, N. A.; Carney, T. J.; Yang, Y.; Cui, Y. Engineering Empty Space between Si Nanoparticles for Lithium-Ion Battery Anodes. *Nano Lett.* **2012**, *12*, 904–909.

- (24) Wu, H.; Yu, G.; Pan, L.; Liu, N.; McDowell, M. T.; Bao, Z.; Cui, Y. Stable Li-ion battery anodes by in-situ polymerization of conducting hydrogel to conformally coat silicon nanoparticles. *Nat. Commun.* **2013**, *4*, 6.
- (25) Chen, X. L.; Li, X. L.; Ding, F.; Xu, W.; Xiao, J.; Cao, Y. L.; Meduri, P.; Liu, J.; Graff, G. L.; Zhang, J. G. Conductive Rigid Skeleton Supported Silicon as High-Performance Li-Ion Battery Anodes. *Nano Lett.* **2012**, *12*, 4124–4130.
- (26) Liu, N.; Wu, H.; McDowell, M. T.; Yao, Y.; Wang, C. M.; Cui, Y. A Yolk-Shell Design for Stabilized and Scalable Li-Ion Battery Alloy Anodes. *Nano Lett.* **2012**, *12*, 3315–3321.
- (27) Chou, S. L.; Wang, J. Z.; Choucair, M.; Liu, H. K.; Stride, J. A.; Dou, S. X. Enhanced reversible lithium storage in a nanosize silicon/graphene composite. *Electrochem. Commun.* **2010**, *12*, 303–306.
- (28) Zhou, X. S.; Yin, Y. X.; Wan, L. J.; Guo, Y. G. Facile synthesis of silicon nanoparticles inserted into graphene sheets as improved anode materials for lithium-ion batteries. *Chem. Commun.* **2012**, *48*, 2198–2200.
- (29) Vankooten, J. J.; Weller, G. A.; Ammerlaan, C. A. J. Electron-Paramagnetic Resonance on Iron-Acceptor Pairs in Silicon. *Phys. Rev. B* **1984**, *30*, 4564–4570.
- (30) Charitidis, C. A.; Skarmoutsou, A.; Nassiopoulou, A. G.; Dragoneas, A. Nanomechanical properties of thick porous silicon layers grown on p- and p plus -type bulk crystalline Si. *Mater. Sci. Eng. A-Struct.* **2011**, *528*, 8715–8722.
- (31) Pei, S. F.; Cheng, H. M. The reduction of graphene oxide. *Carbon* **2012**, *50*, 3210–3228.
- (32) Wang, B.; Li, X.; Qiu, T.; Luo, B.; Ning, J.; Li, J.; Zhang, X.; Liang, M.; Zhi, L. High Volumetric Capacity Silicon-Based Lithium Battery Anodes by Nanoscale System Engineering. *Nano Lett.* **2013**, *13*, 5578–5584.
- (33) Graetz, J.; Ahn, C. C.; Yazami, R.; Fultz, B. Highly reversible lithium storage in nanostructured silicon. *Electrochem. Solid-State Lett.* **2003**, *6*, A194–A197.
- (34) Amine, K.; Liu, J.; Belharouak, I. High-temperature storage and cycling of C-LiFePO₄/graphite Li-ion cells. *Electrochem. Commun.* **2005**, *7*, 669–673.
- (35) Yi, R.; Dai, F.; Gordin, M. L.; Chen, S. R.; Wang, D. H. Micro-sized Si-C Composite with Interconnected Nanoscale Building Blocks as High-Performance Anodes for Practical Application in Lithium-Ion Batteries. *Adv. Energy Mater.* **2013**, *3*, 295–300.
- (36) Yi, R.; Dai, F.; Gordin, M. L.; Sohn, H.; Wang, D. H. Influence of Silicon Nanoscale Building Blocks Size and Carbon Coating on the Performance of Micro-Sized Si-C Composite Li-Ion Anodes. *Adv. Energy Mater.* **2013**, *3*, 1507–1515.